Journal of Materials Chemistry A

Accepted Manuscript

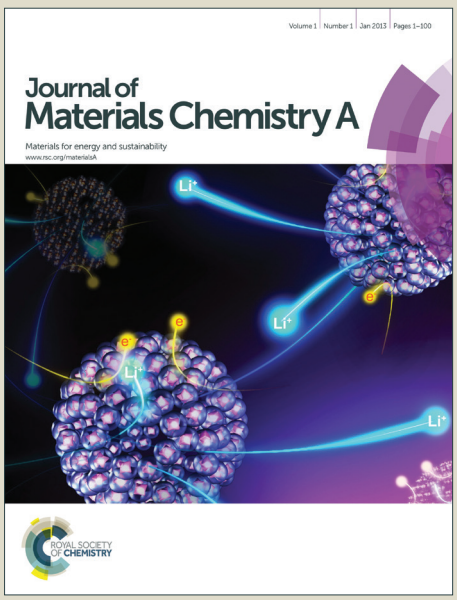

ROYAL SOCIETY OF CHEMISTRY

www.rsc.org/materialsA

Table of Contents

A core-shell nano-scale mixing method is applied to fabricate highly densified $BaTiO_3$/low melting-glass nanocomposite, which appears to be a promising material system for high energy storage capacitor applications.

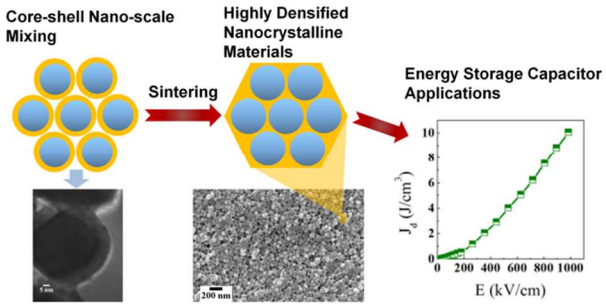

Preparation of $BaTiO_3$/Low Melting Glasses Core-Shell Nanoparticles for Energy Storage Capacitor Applications

Xiaofeng Su[1], Brian C. Riggs[2], Minoru Tomozawa[*1], J. Keith Nelson[3], Douglas B. Chrisey[2]

[1]Department of Materials Science and Engineering, Rensselaer Polytechnic Institute, Troy, NY 12180 USA E-mail: tomozm@rpi.edu

[2]Department of Physics and Engineering Physics, Tulane University, New Orleans, LA 70118 USA

[3]Department of Electrical, Computer and Systems Engineering, Rensselaer Polytechnic Institute, Troy, NY 12180 USA

Abstract:

A core-shell nano-scale mixing technique was applied to fabricate $BaTiO_3$/glass nanocomposites in order to preserve the nano-grain dielectric properties of $BaTiO_3$ after sintering and enhance the bulk composite energy storage capability. Coating layers of low melting glasses of lead borosilicate glass ($65PbO\text{-}20B_2O_3\text{-}15SiO_2$, mol%) and bismuth borosilicate glass ($65Bi_2O_3\text{-}20B_2O_3\text{-}15SiO_2$, mol%) were deposited onto $BaTiO_3$ nanoparticles in chemical solution by a sol-precipitation method under ultrasonic agitation. Transmission electron microscopy (TEM) results confirmed the formation of core-shell nanostructures with controllable shell thicknesses between 2 and 18 nm. X-ray diffraction (XRD) patterns showed that no crystalline peaks were detected from the glass coating layer. Fourier transform infrared (FT-IR) spectra indicated a glass network structure of lead borosilicate glass and bismuth borosilicate glass, respectively. High densifications were achieved for both composites by sintering at low temperatures ($\leq$ 900°C). Noticeable grain growth was observed, however, for lead borosilicate glass-coated $BaTiO_3$ (Pb-BT) composite while almost no grain growth was observed for bismuth borosilicate glass-coated $BaTiO_3$ (Bi-BT) nanocomposite. This disparity was attributed to the different interactions between the $BaTiO_3$ core and two glasses during the sintering process, as revealed by the XRD study. Dielectric properties and energy

storage capability of Bi-BT nanocomposite were investigated in detail. Bi-BT nanocomposite showed high polarization, high dielectric breakdown strength (⩾1000 kV/cm), postponed polarization saturation, and low remnant polarization with the discharge energy density of ~10 J/cm^3 at 1000 kV/cm. Thus, Bi-BT core-shell nanocomposite appears to be a promising material system for energy storage capacitor applications.

1. Introduction

Barium titanate ($BaTiO_3$) has played an important role in the fabrication of multi-layer ceramic capacitors (MLCCs)[1,2], dynamic random access memory (DRAM)[3,4], actuators[5], etc. It exhibits a high polarization value that is desirable for energy storage capacitor applications. The discharge energy density of a dielectric material is given by,

$$J_d = \int_0^{P_{max}} EdP \quad (1)$$

where E is the electric field and P_{max} is the electric polarization at the highest electric field (E_{max}). For linear dielectrics, the expression is simplified as,

$$J_d = \frac{1}{2}\varepsilon_0\varepsilon_r E^2 \quad (2)$$

where ε_0 is the vacuum permittivity and ε_r is the relative permittivity of linear dielectrics. Therefore, the energy density is proportional to the relative permittivity and square of electric field, which is limited by the dielectric breakdown strength (E_b). When a ferroelectric material is employed, the polarization saturation at a field much lower than E_b and high remnant polarization reduce the energy storage quantity. Thus, an optimum dielectric for high energy storage capacitors should possess high polarization, high dielectric breakdown strength, postponed polarization saturation, and low remnant polarization. It is known that the dielectric breakdown strength of ceramic materials has a strong dependence on grain size, with smaller grains giving higher dielectric breakdown strength.[6,7] Furthermore, unlike early polarization saturation of coarse-grained barium titanate, nanocrystalline $BaTiO_3$ (~30 nm) fabricated by spark plasma sintering exhibited a narrow and nearly linear polarization hysteresis loop and postponed polarization saturation.[8,9] Therefore, both the high dielectric breakdown strength and postponed

polarization saturation make nanocrystalline $BaTiO_3$ an attractive material for high energy storage capacitor applications.

It is extremely difficult, in general, to obtain highly densified $BaTiO_3$ with grain size maintained on the nanometer scale (<100 nm) due to the ease of grain growth of nanoparticles. Several fabrication techniques have been explored, such as hot isostatic pressing[10,11], spark plasma sintering[8,9,12], and two-step sintering[13]. However, those methods require either costly equipment or starting materials of mono-dispersed nanoparticles no larger than 10 nm. An alternate method utilizes glass as a sintering agent for ceramic materials to promote densification by viscous flow sintering.[14-18] There are many benefits of adding a glass sintering agent, such as reductions of sintering temperature[14,15] and porosity[16], suppression of grain growth[17], and improvement of dielectric breakdown strength[18]. Thus, an appropriate glass sintering agent addition would help achieve high densification and inhibit grain growth during high temperature heat-treatment. Therefore, $BaTiO_3$/glass nanocomposites appear to be a desirable material system for high energy storage capacitor applications.

When preparing $BaTiO_3$/glass composites, high energy ball milling helps ensure uniform mixing of glass and ceramic powders on the micrometer range. However, when starting with ceramic particles on the nanometer scale, the homogeneous distribution of glass powder (>1 μm) around fine ceramic particles is difficult to achieve using this technique.[19] Furthermore, ball milling often introduces impurities. Here, we applied a core-shell method to coat $BaTiO_3$ nanoparticles with a thin layer of glass to form $BaTiO_3$/glass core-shell nanostructures. This method guarantees uniform mixing of two phases on the nanometer scale. Moreover, this glass coating layer derived from a chemical method is applicable for a variety of different glass compositions. Core-shell nano-ferroelectrics have been recently fabricated by encapsulating $Ba_{1-x}Sr_xTiO_3$ particles in a thin shell of SiO_2.[20-22] By viscous flow of the silica coating layer, sintering temperature of the composite was reduced from 1400°C to 1100°C for pure $Ba_{1-x}Sr_xTiO_3$ particles. This nanocomposite exhibited very low dielectric loss but a rather low dielectric constant as well.[21] No detailed densification or grain growth prevention characteristic of this composite was reported.

Herein we report the deposition of a low melting glass layer of $65PbO\text{-}20B_2O_3\text{-}15SiO_2$ (mol%) or $65Bi_2O_3\text{-}20B_2O_3\text{-}15SiO_2$ (mol%) onto commercial $BaTiO_3$ nanoparticles with average grain size of 55 nm. Both glass compositions were chosen primarily for their low melting characteristics as judged from the phase diagrams of various oxides[23-25]. In addition to the low melting temperatures, both the Pb^{2+} and Bi^{3+} ions possess high polarizability, which contributes to the high dielectric constant (>15) of the glasses[26,27]. Bismuth borosilicate glass was investigated here as a possible replacement for lead borosilicate glass, which may not be usable in practical applications due to the concern of lead toxicity. The objective of this study is to fabricate multi-component glass-coated $BaTiO_3$ core-shell nanoparticles by the sol-precipitation method and further reduce the sintering temperature ($\leq$ 900°C) of the nanocomposites by using low melting glass composition. The specific goal is to produce a highly densified (~99%) $BaTiO_3$/glass nanocomposite at low sintering temperature (~900°C). Then, the dielectric properties and energy storage capability of $BaTiO_3$/low-melting glass nanocomposite will be measured and analyzed for energy storage capacitor applications. Sample thickness is also known to affect dielectric breakdown strength[6,7]. Therefore, in this study, sample thickness was varied for $BaTiO_3$/low-melting glass nanocomposite once the desired microstructure was achieved and their dielectric breakdown strength was investigated.

2. Experimental Procedures

2.1 Materials

A $BaTiO_3$ nanopowder (cubic crystalline phase, <100 nm particle size, ≥ 99% in purity) was purchased from Sigma-Aldrich Co. as the starting material. Transmission electron microscopy (TEM) and scanning electron microscopy (SEM) analysis demonstrated the average diameter of the starting nanoparticles is 55±9 nm with spherical shape.

2.2 Low melting glass coating

The synthesis of core-shell nanoparticles is based upon a sol-precipitation method. The fabrication procedure is shown in Fig. 1 for both glass compositions. The details are described below.

(1) $65PbO\text{-}20B_2O_3\text{-}15SiO_2$ (mol%) glass coating

Triethyl borate (TEB), tetraethyl orthosilicate (TEOS), and lead acetate trihydrate ($Pb(CH_3COO)_2 \cdot 3H_2O$) were used as the precursors for each glass component. All operations were performed at room temperature unless specified otherwise. For a typical fabrication procedure, 500 mg $BaTiO_3$ nanoparticles were added to 190 ml ethanol and 37 ml DI water mixture. Then the suspension was subjected to ultrasonic dispersion for 2 h. This homogeneous distribution is a prerequisite for the uniform coating in the following steps. At the same time, precursor solutions were prepared separately. A mixture of 79 μl of TEB and 39 μl of TEOS was added to 10 ml ethanol solution during magnetic stirring. After mixing for 10 mins, 1 ml of DI water was added for the hydrolysis of TEB and TEOS at 65°C. After 1 h reaction, this solution was ready for coating and named the borosilicate precursor solution. In the meantime, the lead precursor solution was prepared by dissolving 288 mg $Pb(CH_3COO)_2 \cdot 3H_2O$ in 2 ml DI H_2O. Both borosilicate precursor and lead precursor solutions were added to the $BaTiO_3$ base solution while vigorously stirring to form a uniform distribution surrounding the core nanoparticles. Then 5 ml ammonia hydroxide solution (28% NH_3 in H_2O) was added to initiate the precipitation of each glass component onto the $BaTiO_3$ bare particles while simultaneously magnetic stirring and ultrasonically agitating. After the reaction was completed, the mixture solution was centrifuged and the resulting nanoparticles were collected and dried at 150°C for 3 h.

(2) $65Bi_2O_3$-$20B_2O_3$-$15SiO_2$ (mol%) glass coating

For the bismuth borosilicate glass coating, TEB, TEOS, and bismuth nitrate pentahydrate ($Bi(NO_3)_3 \cdot 5H_2O$) were used as the precursors. Since $Bi(NO_3)_3 \cdot 5H_2O$ cannot dissolve in ethanol, ethylene glycol (EG) was used as the dispersion medium instead. Similar to the lead borosilicate glass coating, 500 mg $BaTiO_3$ nanoparticles were first dispersed in 190 ml EG and 37 ml H_2O mixture under ultrasonic agitation for 2 h. A mixture of 45 μl of TEB and 22 μl of TEOS was dissolved in 10 ml ethanol for uniform distribution, which was followed by the addition of 1 ml H_2O for hydrolysis. After 1 h reaction, the solution was ready for coating and designated the borosilicate precursor solution. A bismuth precursor solution was produced by dissolving 420 mg $Bi(NO_3)_3 \cdot 5H_2O$ in 4 ml DI water and 0.8 ml nitric acid mixture. Then, both borosilicate precursor and bismuth precursor solutions were added to the

$BaTiO_3$ dispersion for uniform distribution. By adding 5 ml ammonia hydroxide solution, the coating process was initiated. At the end of the reaction, the mixture solution was centrifuged and the product was collected and dried at 150°C for 3 h.

2.3. Sintering

The $BaTiO_3$ nanoparticles coated with glass layer were mixed with 4 wt% polyvinyl alcohol binder solution and pressed into pellets with diameter of 13 mm and thickness of 1 mm under a pressure of 200 MPa. Those pellets were subjected to binder removal heat-treatment at 500°C for 1 h which was followed by isothermal sintering at a series of temperatures of 600-900°C for 2 h each and air cooled afterwards. Coarse-grained barium titanate (C-BT) was also prepared for comparison by a two-step sintering method: the green compact of pure $BaTiO_3$ nanoparticles was heated to 1225°C at 15°C/min, cooled to 1100°C at 30°C/min immediately, and held at 1100°C for 20 h.

2.4. Characterization

The morphology of the core-shell nanoparticles was investigated by transmission electron microscopy (JEM-2011, JEOL Ltd., Tokyo, Japan). Crystal structures and phase compositions of coated nanoparticles and sintered pellets were studied by X-ray diffraction (XRD) using a diffractometer (X'pert Pro., PANalytical, Almelo, Netherland) with Cu Kα radiation (λ=1.5406 Å). Fourier transform infrared spectroscopy (FT-IR) analysis was performed on core-shell nanoparticles using a spectrometer (Nicolet Magna 560, Nicolet Instrument, Inc., Madison, WI, USA) by KBr method to study the glass network structure of each coating. The densities of pellets after sintering were measured by both the Archimedes method and sample dimensions. The microstructures of sintered samples were studied using a field emission scanning electron microscope (SUPRA 55, Carl Zeiss Microscopy, Thornwood, NY, USA). For electrical measurements, sintered pellets were polished and coated with silver paste on both sides with electrode area of 28 mm^2. The further thinning of bismuth borosilicate glass-coated $BaTiO_3$ (Bi-BT) nanocomposite was accomplished by a precision polisher (Multiprep Polishing System-8″, Allied High Tech Products, Inc., Rancho Dominguez, CA, USA) in order to investigate the sample thickness dependence of dielectric breakdown strength. The relative permittivity and

loss tangent were then characterized using a RLC Digibridge (RLC 1689 Tester, IET Labs, Inc., Westbury, NY, USA). Over 10 samples were prepared for DC dielectric breakdown strength measurement at room temperature with voltage ramp rate of 10 kV/min using a high voltage DC power supply (8100-10, Hipotronics, Inc., Brewster, NY, USA). Samples were immersed in silicone oil to avoid surface flashover. The polarization-electric field P(E) hysteresis loops were measured using a ferroelectric tester (Precision Premier II, Radiant Technologies, Inc., Albuquerque, NM, USA) under a triangular waveform of different amplitudes at 50 Hz.

3. Results and Discussion

3.1 Investigation of core-shell nanoparticles

Fig. 2 shows the $BaTiO_3$ core-shell nanostructures coated with low melting glasses from different precursor solutions with various concentrations. Since the heavy elements, Pb or Bi, were contained in the coating layer, the contrast between the core and shell is not as clear as the core-shell nanoparticles reported for titanate/SiO_2 glass in the literature[20-22]. But a careful observation of Fig. 2 (a) and Fig. 2 (b) for $BaTiO_3$/lead borosilicate glass reveals that a uniform and smooth coating layer was obtained by the sol-precipitation method. Very few (<10%) isolated glass particles were present in the dispersion. Similarly, Fig. 2 (c) and Fig. 2 (d) exhibit the coating morphology of bismuth borosilicate glass. The coating results can be affected by many parameters, such as temperature, pH value, reaction time, and precursor concentrations.[28,29] But a simple way to change the coating thickness is to vary the precursor concentrations. For example, the precursor concentrations for Fig. 2 (c) are $9.1x10^{-3}$ M $Bi(NO_3)_3 \cdot 5H_2O$, $2.8x10^{-3}$ M TEB, and $1.1x10^{-3}$ M TEOS while the precursor concentrations for Fig. 2 (d) are $3.2x10^{-3}$ M $Bi(NO_3)_3 \cdot 5H_2O$, $9.9x10^{-4}$ M TEB, and $3.7x10^{-4}$ M TEOS. With the decreasing precursor concentration, the shell thickness was reduced from 9 nm to 2~3 nm, which was the thinnest shell thickness that was achieved in this study and is shown in Fig. 2 (d).

In the application that we are pursuing, the shell thickness should be well controlled in order to tailor the volume fraction of the glass phase, which has a great influence on the dielectric properties of the nanocomposites. The glass addition should be large enough to fill the voids or pores of the $BaTiO_3$ nanoparticles packing

but not too large to unnecessarily reduce the high dielectric constant of the composite. Assuming that the starting $BaTiO_3$ nanoparticles are perfect spheres with diameter of 55 nm, a close packing density should be 0.74, which requires 26 vol% of glass addition to reach full densification when no grain growth is assumed to take place during the sintering process. This densification mechanism mainly depends on the grain rearrangements instead of dissolution-precipitation that is closely related to grain growth.[30] Under these circumstances, a geometric calculation leads to the coating thickness of 2.6 nm which is called the optimum glass coating thickness. Based on the density of each glass component and the linear mixing rule, the amount of precursor solution needed to deposit a 2.6 nm coating layer was calculated and prepared. A comparison between the theoretical calculation (2.6 nm) and the experimental result (2~3 nm in Fig. 2 (d)) indicates that the rule of precursor chemical estimation is reasonably accurate. Core-shell nanoparticles with optimum glass coating layer (2.6 nm thick, 26 vol%) were applied for the following characterization.

Fig. 3 exhibits the XRD patterns of (a) lead borosilicate glass-coated $BaTiO_3$ (Pb-BT) nanoparticles and (b) bismuth borosilicate glass-coated $BaTiO_3$ (Bi-BT) nanoparticles. As shown in Fig. 3, all the crystalline peaks are derived from the $BaTiO_3$ raw materials and no other crystalline phase peak was observed due to the coating layer. The small peaks detected around 24° and 28° in Pb-BT nanoparticles were attributed to $BaCO_3$ impurity from pristine commercial $BaTiO_3$, which was confirmed by the FT-IR data later. A broad peak around 28° in Bi-BT nanoparticles was observed, which is a typical feature of amorphous material. The absence of carbonate peaks in Bi-BT nanoparticles will be explained later.

In order to study the glass network structure of the coating layers in both cases, FT-IR spectra of $BaTiO_3$ nanoparticles before and after coating are shown in Fig. 4. We focused on the mid infrared region (400~2000 cm^{-1}) where the vibration modes of lead borosilicate glasses or bismuth borosilicate glasses are active.

For Pb-BT, the sharp absorption band at 572 cm^{-1}, which was observed both before and after coating, was due to the Ti-O vibrations of barium titanate[31]. In addition, another absorption band near 1440 cm^{-1} originates from the stretching vibrations of –

CO_3^{2-} due to the residual $BaCO_3$ in the raw material $BaTiO_3$[32]. This absorption band, however, was not detected in Bi-BT, which could be explained by the addition of nitric acid during bismuth borosilicate glass-coated $BaTiO_3$ nanoparticles preparation. The small amount of nitric acid, which was used to promote the dissolution of $Bi(NO_3)_3 \cdot 5H_2O$, reacted with $BaCO_3$ and removed $BaCO_3$ in the final product. Except for the characteristic peaks of pristine $BaTiO_3$, two broad bands at 800-1000 cm^{-1} and 1300-1400 cm^{-1} were observed for Pb-BT. The broad band between 800 and 1000 cm^{-1} could be attributed to the overlapping of absorption bands at 880 cm^{-1}, 915 cm^{-1}, and 950 cm^{-1}, which correspond to the vibrations of the B-O-Pb network[33], Si-O-B stretching[34], and Si-O-Pb stretching[33], respectively. The absorption band around 1400 cm^{-1} indicates the stretching vibrations of B-O bonds while the weak shoulder at 1350 cm^{-1} was due to the B-O-B linkages.[35,36] The glass network structures of lead borosilicate glasses have been studied extensively.[33,37,38] It is indicated that in lead borosilicate glass systems, PbO works as a glass modifier at low concentrations and acts as a glass former at high concentrations.[38] The presence of 880 cm^{-1} and 950 cm^{-1} bands demonstrated that PbO was incorporated into the borosilicate glass network and reconstructed the network by the B-O-Pb and Si-O-Pb bonds formation during the sol-precipitation fabrication.

For Bi-BT also, Ti-O vibrations of $BaTiO_3$ before and after coating are confirmed from the absorption band at 572 cm^{-1}. After the coating process, several absorption bands come up reflecting the glass network structure of the coating layer. The stretching vibrations of Bi-O bonds in BiO_6 units were determined from the 490 cm^{-1} and 860 cm^{-1} absorption bands[39-41]. The absorption band near 880 cm^{-1} was assigned to be the stretching vibrations of B-O bonds in BO_4 units that were overlaid with symmetric stretching vibrations of Bi-O bonds in BiO_3 units[39]. The presence of stretching vibrations of B-O bonds in BO_4 units and stretching vibrations of Si-O bonds were confirmed by the FT-IR absorption bands at 1060 cm^{-1} [42]and 1100 cm^{-1} [35], respectively. In addition, the vibration bands of B-O-B linkages[35] or B-O bonds[43] were also labeled. The bismuth oxide-based glass system as a replacement for the lead oxide-based glass system has attracted many structural studies. Bismuth oxide is not a classical network former because of the high polarizability and small field

strength of Bi^{3+}. However, glass formation becomes possible for a wide range of compositions with the presence of B_2O_3[44]. It has been found that Bi-O could take the form of either distorted BiO_6 units[45] or BiO_3 polyhedra[46] in a bismuth borate glass network. Overall, the FT-IR results confirmed the coating layer structure as lead borosilicate glass or bismuth borosilicate glass.

Combining the results of TEM, XRD, and FT-IR, it was confirmed that the sol-precipitation method is a viable technique to fabricate $BaTiO_3$/lead borosilicate glass core-shell nanoparticles and $BaTiO_3$/bismuth borosilicate glass core-shell nanostructures.

3.2 Sintering study

It is known that glass in glass/ceramic composites promotes viscous flow sintering, improves densification, and effectively reduces grain size of composite materials. The optimum sintering temperature for each glass-coated $BaTiO_3$ nanocomposite was investigated by sintering at a series of temperatures and measuring densities of the sintered pellets. The optimum sintering temperature is defined as the lowest temperature that can produce high densification. In order to achieve a low sintering temperature, heat-treatment temperatures in this study were chosen to be no higher than 900°C. Fig. 5 shows the density of each nanocomposite after sintering at a series of temperatures for 2 h each. As shown in Fig. 5, the density of Pb-BT composite saturated at 700°C while the density of Bi-BT nanocomposite kept increasing up to 900°C. Therefore, the optimum sintering temperature of Pb-BT composite and Bi-BT nanocomposite was determined to be 700°C and 900°C, respectively. The low sintering temperature of less than 1000°C helps to reduce the production cost and makes the use of base metal electrodes such as copper and nickel possible[47].

After the optimum sintering treatment, the fracture surface of each sintered pellet was observed under SEM as shown in Fig. 6. The Pb-BT composite in Fig. 6 (a) exhibited appreciable grain growth with some grains growing up to 2~3 μm while the starting grain size was 55 nm. It seems that the lead borosilicate glass coating layer could not prevent the grain growth of $BaTiO_3$ nanoparticles during sintering. In contrast, almost no grain growth was observed for Bi-BT nanocomposite in Fig. 6 (b) with all the grains maintained on the nanometer scale (55~65 nm). This grain growth

inhibition even for adjacent grains in Bi-BT nanocomposite suggests that a thin diffusion barrier layer was formed between nano-grains, effectively suppressing the grain boundary migration during the sintering process. To further illustrate this point, pure $BaTiO_3$ was sintered for comparison at the same temperature as Bi-BT nanocomposite (900°C for 2 h). The fracture surface of pure $BaTiO_3$ shown in Fig. 6 (c) indicates poor densification together with apparent grain growth, which results from the absence of a coating barrier. Moreover, Bi-BT nanocomposite exhibited fully densified microstructures as shown in Fig. 6 (b): the "pore-like" voids are attributed to the grains that were pulled out during fracture. Therefore, the bismuth borosilicate glass coating on $BaTiO_3$ was demonstrated to be an effective densification promoter and grain growth inhibitor. High densification was achieved and nano-grain size (~60 nm) was maintained thanks to the bismuth borosilicate glass coating layer.

The XRD patterns of sintered samples are shown in Fig. 7. A good glass sintering agent should lead to small amount of second phases after sintering such that the dielectric properties of the original ceramic phase is preserved. For Pb-BT composite, Pb substituted Ba in $BaTiO_3$ and transformed the $BaTiO_3$ phase completely into solid solution $Ba_xPb_{1-x}TiO_3$ phase as shown in Fig. 7(a). The chemical substitution of Pb into the $BaTiO_3$ lattice modifies the dielectric properties of $BaTiO_3$, according to previous studies[48,49]. In addition to Pb substitution for Ba, formation of Ba_2SiO_4 was also observed due to the reaction between the glass layer and ceramic core, together with trace amount of PbO crystallites formation as shown in the XRD pattern. The peak splitting of (200) and (002) at 45° indicates a tetragonal structure of $Ba_xPb_{1-x}TiO_3$, which was caused by both Pb substitution and noticeable grain growth as observed in Fig. 6 (a). On the other hand, there is no Bi substitution in $BaTiO_3$ observed for Bi-BT nanocomposite with the original cubic $BaTiO_3$ maintained as the primary crystalline phase. Secondary phase $Bi_{12}TiO_{20}$ was formed during the sintering process, as shown in Fig. 7 (b).

The secondary crystalline phase $Bi_{12}TiO_{20}$ detected in Bi-BT nanocomposite can be understood by postulating the interfacial reaction between $BaTiO_3$ core and bismuth boroslicate glass shell as shown in equation (3).

$$BaTiO_3 + 6Bi_2O_3 \rightarrow Bi_{12}TiO_{20} + BaO \quad (3)$$

Since the volume percent of the glass coating shell is controlled at 26 %, the molecular ratio of $BaTiO_3$ to $0.65Bi_2O_3$-$0.20B_2O_3$-$0.15SiO_2$ glass is calculated to be 76/24 assuming that the glass can be considered as a big molecule. According to equation (3), 24 mol glasses that contain 15.6 mol Bi_2O_3 would consume 2.6 mol $BaTiO_3$ out of 76 mol in the interfacial reaction when all the Bi_2O_3 took part in the reaction. It is important to note that this amount of $BaTiO_3$ only accounts for the outer thin shell with the thickness of 0.6 nm of a 55 nm grain, which suggests that the dielectric properties of nano-grained $BaTiO_3$ would be mostly retained. Details of the above calculation is shown below,

Number of Moles	$BaTiO_3$	+ $6Bi_2O_3$	→ $Bi_{12}TiO_{20}$	+ BaO
Initial	76	15.6	0	0
Reacted	-2.6	-15.6	2.6	2.6
End	73.4	0	2.6	2.6

In addition, the effect of interfacial reaction on the relative density of Bi-BT nanocomposite can be evaluated. Before interfacial reaction, Bi-BT nanocomposite consists of $BaTiO_3$ core and Bi_2O_3-B_2O_3-SiO_2 shell and its theoretical density is estimated by the linear mixing rule that combines the individual densities of each glass component and pure $BaTiO_3$ (ρ = 6.02 g/cm^3), which is determined to be 6.39 g/cm^3. When interfacial reaction takes place with all the Bi_2O_3 taking part in the reaction, Bi-BT nanocomposite would be composed of $BaTiO_3$ core, interfacial compound $Bi_{12}TiO_{20}$ (ρ = 8.95 g/cm^3)[50], and remaining glass shell (BaO-B_2O_3-SiO_2, ρ = 3.15 g/cm^3)[51]. Here, an assumption was made that the interfacial reaction product BaO goes into the glass shell and forms BaO-B_2O_3-SiO_2 glass, which seems to be reasonable since no BaO crystalline phase was detected in Fig. 7 (b). The volume fractions of each phase were calculated according to equation (3) and the theoretical density was estimated to be 6.41 g/cm^3. Since the sintered Bi-BT nanocomposite density was measured to be 6.32 g/cm^3, the calculated relative density of Bi-BT nanocomposite after sintering changes from 98.9% to 98.6% when interfacial reaction takes place. Therefore, interfacial reaction has slight effect on the relative density

calculation of Bi-BT nanocomposite. This demonstrates that Bi-BT nanocomposite sintered at 900°C was highly densified (~99%).

The observed disparity of microstructures and crystalline phase developments for Pb-BT composite and Bi-BT nanocomposite can be attributed to the different interactions between $BaTiO_3$ and two glass coatings. Pb^{2+} was demonstrated to be a highly soluble cation in perovskite titanates due to its compatible size and charge with Ba^{2+}.[52] The Pb substitution shifted up the Curie temperature and decreased the dielectric constant of barium titanate at room temperature significantly[53], which is not desirable in this study. The Pb substitution can be accomplished by either diffusion of Pb into $BaTiO_3$ lattice[49] or dissolution of $BaTiO_3$ into glass phase and re-precipitation of $Ba_xPb_{1-x}TiO_3$ that contributes to the extensive grain growth[54,55]. Earlier study of $BaTiO_3$ interfacial reaction with $PbO\text{-}B_2O_3$ glasses demonstrated that the growth kinetics of the $Ba_xPb_{1-x}TiO_3$ perovskite exhibits a linear time dependence, which suggests the dissolution-reprecipitation mechanism[55]. In contrast, Bi^{3+} cannot be easily incorporated into a $BaTiO_3$ lattice without the presence of other cations such as Cd^{+} to balance the charge.[52] Microstructures in Fig. 6 (b) demonstrated no apparent dissolution of $BaTiO_3$ in the bismuth borosilicate glass and that most grains remained the original shape and size. Previous research[48,49] reported that intergranular phases were formed due to the interfacial reaction between $BaTiO_3$ and $Bi_2O_3\text{-}B_2O_3$ binary glass with Bi_2O_3-rich glass compositions, consistent with the XRD observation in this study. The second phase $Bi_{12}TiO_{20}$ together with the remaining glass phase sitting between grain boundaries of $BaTiO_3$ played an important role in grain growth suppression[56]. Overall, bismuth borosilicate glass is a better sintering agent compared to lead borosilicate glass in terms of the preservation of $BaTiO_3$ nano-grain size.

3.3 Dielectric properties

In view of the preservation of nano-grain $BaTiO_3$ in Bi-BT nanocomposite, the subsequent dielectric and energy storage measurements were performed exclusively on this material system. The dielectric constant and loss tangent of Bi-BT nanocomposite after sintering are shown in Fig. 8. At room temperature, the dielectric constant of Bi-BT nanocomposite is around 560 at 1 kHz as shown in Fig. 8 (a), which is lower than that of coarse-grained $BaTiO_3$ (ε_r>1000) mainly due to the

dilution effect of glass addition and the intrinsic size effects of $BaTiO_3$[57,58]. The Curie temperature, which represents the ferroelectric-paraelectric transition, decreased from the bulk value (130 ℃) to approximately 72 ℃ for Bi-BT nanocomposite, which was determined to be the temperature of permittivity maximum. The permittivity peak was broadened and rounded, which shows better temperature stability compared to coarse-grained $BaTiO_3$[59]. The variance of permittivity value from room temperature to 110 ℃ is within ±10% of the room temperature value. The grain size dependence of Curie temperature and relative permittivity for ferroelectric particles was studied by using Landau phenomenological theory[60]. The decreasing trend of Curie temperature and polarization value with decreasing grain size was simulated by introducing a surface term and a gradient term in the total free energy expression. It is important to note that this grain size effect is closely related to the surface or interface of ferroelectric materials, which explains the different dielectric behaviors observed in various systems such as, ferroelectric particles[61], sintered ceramics[9,58], ceramic/glass composites[14-17] and glass-ceramics[57].

Fig. 8 (b) shows the dielectric loss of Bi-BT nanocomposite from room temperature to 110°C. As can be seen, the Bi-BT nanocomposite exhibits dielectric loss with most values ≤1 %, which indicates good dielectric quality of the material[58].

Fig. 9 shows the Weibull plot of dielectric breakdown strength in Bi-BT nanocomposite with different thicknesses. A weibull plot is usually used to analyze the breakdown strength of dielectric materials because of its statistical nature of failure. The Weibull modulus m, which is the slope of the plot, describes the distribution of dielectric breakdown strength and was found to be 10.4 and 6.9 for samples with thickness of 300 μm and 12 μm, respectively. The characteristic dielectric breakdown strength, which corresponds to the dielectric breakdown strength at 63 % failure probability, was determined to be 390 kV/cm and 1140 kV/cm for Bi-BT nanocomposite with thickness of 300 μm and 12 μm, respectively. Compared with bulk $BaTiO_3$ ceramic (~100 kV/cm) with grain size on the micrometer range and thickness of 200 μm[62], the dielectric breakdown strength of Bi-BT nanocomposite is remarkably improved, which could be attributed to the higher densification and smaller grain size obtained in the material in the present study. It is

known that dielectric breakdown strength has a strong dependence on sample thickness, with thinner samples giving higher breakdown strength[6,7,63]. In this study, Bi-BT nanocomposite with thickness of 12 μm exhibited a higher breakdown strength of 1140 kV/cm, consistent with the observed trends[6,7,63].

3.4 Energy Storage Capability

The energy storage capability of Bi-BT nanocomposite with 16 μm thickness was evaluated by P-E tests. For comparison, P(E) hysteresis loops of a coarse-grained barium titanate (C-BT) prepared by two-step sintering having an average grain size of 560 nm and thickness of 250 μm were also measured. Fig. 10 (a) exhibits P(E) hysteresis loops of C-BT and Bi-BT nanocomposite under different electric fields. In the inset of Fig. 10 (a), C-BT shows normal ferroelectric switching behavior with remnant polarization (P_r) ~11.6 μC/cm^2 and apparent polarization saturation was observed below 50 kV/cm. In contrast, the P(E) loops of Bi-BT nanocomposite are nearly linear under low electric field up to 400 kV/cm and a deviation from linearity was observed under high electric field above 400 kV/cm. The suppression of ferroelectric switching and the linear polarization loop of dense nanocrystalline $BaTiO_3$ were first observed by Buscaglia, et al[8] in 2006. The polarization suppression of nanocrystalline $BaTiO_3$ was closely related to (i) the decrease of the local electric field due to the presence of low-permittivity grain boundaries and (ii) the pinning of domain wall movements and hindrance of domain switching resulting from the grain boundaries or the defects sitting at the grain boundaries[8,9]. The behavior of Bi-BT nanocomposite in this study is quite similar to that of nanocrystalline $BaTiO_3$ except that the interface layer between $BaTiO_3$ and glass was suppressing the domain switching instead of grain boundaries. Moreover, the nonlinear P(E) loops of Bi-BT nanocomposite under high electric field (>400 kV/cm) demonstrates that ferroelectric switching at nanoscale can be accomplished by the very high electric field.

Finally, the energy storage density of C-BT and Bi-BT nanocomposite, calculated from P(E) loops, was plotted and compared in Fig. 10 (b). The energy storage density of Bi-BT nanocomposite was increasing approximately parabolically with electric field while that of coarse-grained barium titanate was initially rising parabolically and then slows down after 20 kV/cm due to the apparent polarization saturation. The early

polarization saturation limits further energy storage of C-BT under higher electric fields while the postponed polarization saturation and low P_r ~5.4 μC/cm^2 of Bi-BT nanocomposite play an important role in improving energy storage density. As shown in equation (2), energy storage density is proportional to dielectric constant and square of electric field for a linear dielectric. Although Bi-BT nanocomposite behaves as a nonlinear dielectric, its effective dielectric constant can be calculated by parabolic fitting of J_d-E curve as shown in Fig. 10 (b). The effective dielectric constant of Bi-BT nanocomposite was estimated to be 256, which is about one half of the low field permittivity. The highest energy density of Bi-BT nanocomposite obtained in this study is about 10 J/cm^3 at 1000 kV/cm, which is over 80 times that of C-BT. Although the real energy density can be affected by the surface area of capacitor in industrial applications[64], Bi-BT nanocomposite which exhibits both high polarization and high dielectric breakdown strength is demonstrated to be a promising material system for energy storage capacitor applications.

4. Conclusions

$BaTiO_3$/PbO-B_2O_3-SiO_2 and $BaTiO_3$/Bi_2O_3-B_2O_3-SiO_2 ceramic core-glass shell nanoparticles were successfully prepared by the sol-precipitation method. The glass coating layer thickness can be adjusted by the precursor concentrations. Low temperature sintering (~900°C) of Bi-BT nanocomposite exhibited high densification (~99% of theoretical density) but no noticeable grain growth with the optimum glass loading of 26 vol%. It proves that the interfacial compound and glass coating layer work as a diffusion barrier to prevent grain growth during the sintering process. As a result, Bi-BT nanocomposite exhibited postponed polarization saturation and high dielectric breakdown strength (≥1000 kV/cm), which are beneficial to energy storage improvement. The highest energy density obtained by Bi-BT nanocomposite was ~10 J/cm^3 at 1000 kV/cm, which is promising for energy storage capacitor applications. Finally, the encouraging coating results of multi-component and low-melting glasses in this study open up the avenue of precipitating various glass systems onto different ceramics to fabricate new functional materials with designable properties. Moreover, the promising sintering results suggest that the core-shell nano-scale mixing creates a new way to fabricate highly densified (≥99%) nanocrystalline ceramic materials (<100 nm).

Acknowledgements

This research was supported by NSF-EFRI Grant 1038272. The X-ray multipurpose diffractometer used in the present research was acquired through MRI award DMR 0821536.

5. References

1 C.-S. Hsi, Y.-C. Chen, H. Jantunen, M.-J. Wu and T.-C. Lin, *J. Eur. Ceram. Soc.*, 2008, **28**, 2581-2588.

2 S.-G. Kwon, K. Choi and B.-I. Kim, *Mater. Lett.*, 2006, **60**, 979-982.

3 T. Kuroiwa, Y. Tsunemine, T. Horikawa, T. Makita, J. Tanimura, N. Mikami and K. Sato, *Jpn. J. Appl. Phys.*, 1994, **33**, 5187-5191.

4 K. Takemura, S. Yamamichi, P.-Y. Lesaicherre, K. Tokashiki, H. Miyamoto, H. Ono, Y. Miyasaka and M. Yoshida, *Jpn. J. Appl. Phys.*, 1995, **34**, 5224-5229.

5 K. Abe, K. Uchino and S. Nomura, *Ferroelectrics*, 1986, **68**, 215-223.

6 Y. Ye, S. C. Zhang, F. Dogan, E. Schamiloglu, J. Gaudet, P. Castro, M. Roybal, M. Joler and C. Christodoulou, *Proc. 14th IEEE Int. Pulsed Power Con.*, 2003, **1**, 719-722.

7 H. Y. Lee, K. H. Cho and H.-D. Nam, *Ferroelectrics*, 2006, **334**, 165-169.

8 M. T. Buscaglia, M. Viviani, V. Buscaglia, L. Mitoseriu, A. Testino, P. Nanni, Z. Zhao, M. Nygren, C. Harnagea, D. Piazza and C. Galassi, *Phys. Rev. B*, 2006, **73**, 064114.

9 L. Curecheriu, S.-B. Balmus, M. T. Buscaglia, V. Buscaglia, A. Ianculescu and L. Mitoseriu, *J. Am. Ceram. Soc.*, 2012, **95**, 3912-3921.

10 G. Arlt, D. Hennings and G. de With, *J. Appl. Phys.*, 1985, **58**, 1619-1625.

11 A. V. Polotai, A. V. Ragulya and C. A. Randall, *Ferroelectrics*, 2003, **288**, 93-102.

12 S. Yoon, J. Dornseiffer, Y. Xiong, D. Grüner, Z. Shen, S. Iwaya, C. Pithan and R. Waser, *J. Eur. Ceram. Soc.*, 2011, **31**, 1723-1731.

13 X.-H. Wang, X.-Y. Deng, H.-L. Bai, H. Zhou, W.-G. Qu, L.-T. Li and I.-W. Chen, *J. Am. Ceram. Soc.*, 2006, **89**, 438-443.

14 A. Young, G. Hilmas, S. C. Zhang and R. W. Schwartz, *J. Am. Ceram. Soc.*, 2007, **90**, 1504-1510.

15 H.-I. Hsiang, C.-S. Hsi, C.-C. Huang and S.-L. Fu, *J. Alloy Compd.*, 2008, **459**, 307-310.

16 X. Su, M. Tomozawa, J. K. Nelson and D. B. Chrisey, *J. Mater. Sci. Mater. Electron.*, 2013, **24**, 2135-2140.

17 J. C. C. Lin and W.-C. J. Wei, *J. Electroceram.*, 2010, **25**,179-187.

18 V. S. Puli, A. Kumar, R. S. Katiyar, X. Su, C. M. Busta, D. B. Chrisey and M. Tomozawa, *J. Non-Cryst. Solids*, 2012, **358**, 3510-3516.

19 A. Bassano, V. Buscaglia, M. Sennour, M. T. Buscaglia, M. Viviani and P. Nanni, *J. Nanopart. Res.*, 2010, **12**, 623-633.

20 C. Huber, M. Treguer-Delapierre, C. Elissalde, F. Weill and M. Maglione, *J. Mater. Chem.*, 2003, **13**, 650-653.

21 C. Huber, C. Elissalde, V. Hornebecq, S. Mornet, M. Treguer-Delapierre, F. Weill and M. Maglione, *Ceram. Int.*, 2004, **30**, 1241-1245.

22 Y. Gao, A. Elsukova and D. C. Lupascu, *Part. Part. Syst. Charact.*, 2013, **30**, 832-836.

23 R. F. Geller and E. N. Bunting, *J. Research Natl. Bur. Standards*, 1939, **23**, 275-283.

24 E. M. Levin and R. S. Roth, *J. Research Natl. Bur. Standards*, 1964, **68A**, 197-206.

25 E. M. Levin and C. L. McDaniel, *J. Am. Ceram. Soc.*, 1962, **45**, 355-360.

26 J. -M. Wu and H. -L. Huang, *J. Non-Cryst. Solids*, 1999, **260**, 116-124.

27 G. Paramesh and K. B. R. Varma, *Int. J. Appl. Glass Sci.*, 2011, **2**, 235-242.

28 T. Ung, L. M. Liz-Marz án and P. Mulvaney, *Langmuir*, 1998, **14**, 3740-3748.

29 Y. Yin, Y. Lu, Y. Sun and Y. Xia, *Nano Lett.*, 2002, **2**, 427-430.

30 R. M. German, P. Suri and S. J. Park, *J. Mater. Sci.*, 2009, **44**, 1-39.

31 Y. Gao, V. V. Shvartsman, A. Elsukova and D. C. Lupascu, *J. Mater. Chem.*, 2012, **22**, 17573-17583.

32 X. Zhang, H. Chen, Y. Ma, C. Zhao and W. Yang, *Appl. Surf. Sci.*, 2013, **277**, 121-127.

33 E. Mansour, *J. Non-Cryst. Solids*, 2012, **358**, 454-460.

34 M. A. Villegas and J. M. Fern ández Navarro, *J. Mater. Sci.*, 1988, **23**, 2464-2478.

35 J. Y. Kim and P. N. Kumta, *J. Phys. Chem. B*, 1998, **102**, 5744-5753.

36 M. Nogami and Y. Moriya, *J. Non-Cryst. Solids*, 1982, **48**, 359-366.

37 Y. Cheng, H. Xiao, W. Guo and W. Guo, *Ceram. Int.*, 2007, **33**, 1341-1347.

38 P. J. Bray, A. E. Geissberger, F. Bucholtz and I. A. Harris, *J. Non-Cryst. Solids*, 1982, **52**, 45-66.

39 I. Ardelean, S. Cora and V. Ioncu, *J. Optoelectron. Adv. M.*, 2006, **8**, 1843-1847.

40 S. Bale, S. Rahman, A. M. Awasthi and V. Sathe, *J. Alloy Compd.*, 2008, **460**, 699-703.

41 P. Pascuta, L. Pop, S. Rada, M. Bosca and E. Culea, *J. Mater. Sci. Mater. Electron.*, 2008, **19**, 424-428.

42 M. Toderaş, S. Filip and I. Ardelean, *J. Optoelectron. Adv. M.*, 2006, **8**, 1121-1123.

43 P. Vasantharani and N. Sangeetha, *Int. J. Res. Pure Appl. Phys.*, 2013, **3**, 1-6.

44 W. H. Dumbaugh, *Phys. Chem. Glasses*, 1986, **27**, 119-123.

45 V. Dimitrov, Y. Dimitriev and A. Montenero, *J. Non-Cryst. Solids*, 1994, **180**, 51-57.

46 S. Hazra and A.Ghosh, *Phys. Rev. B*, 1995, **51**, 851-856.

47 C. Sun, X. Wang and L. Li, *Ceram. Int.*, 2012, **38S**, S49-S52.

48 Y. Kuromitsu, S. F. Wang, S. Yoshikawa and R. E. Newnham, *J. Am. Ceram. Soc.*, 1994, **77**, 493-498.

49 Y. Kuromitsu, S. F. Wang, S. Yoshikawa and R. E. Newnham, *J. Am. Ceram. Soc.*, 1994, **77**, 852-856.

50 D. J. Santos, L. B. Barbosa, R. S. Silva and Z. S. Macedo, *Adv. Condens. Matter Phys.*, 2013, **2013**, 536754.

51 E.-S. Lim, B.-S. Kim, J.-H Lee and J.-J Kim, *J. Eur. Ceram. Soc.*, 2007, **27**, 825-829.

52 I. Burn, *J. Mater. Sci.*, 1982, **17**, 1398-1408.

53 G. Shirane and K. Suzuki, *J. Phys. Soc. Jpn.*, 1951, **6**, 274-278.

54 T. Yamaguchi, H. Ayaki and L. Asai, *J. Am. Ceram. Soc.*, 1993, **76**, 993-997.

55 A. Hirata and T. Yamaguchi, *J. Am. Ceram. Soc.*, 1997, **80**, 79-84.

56 A. S. Janitzki, B. Hoffmann and P. Gerthsen, *J. Am. Ceram. Soc.*, 1979, **62**, 422-424.

57 D. McCauley, R. E. Newnham and C. A. Randall, *J. Am. Ceram. Soc.*, 1998, **81**, 979-987.

58 Z. Zhao, V. Buscaglia, M. Viviani, M. T. Buscaglia, L. Mitoseriu, A. Testino, M. Nygren, M. Johnsson and P. Nanni, *Phys. Rev. B*, 2004, **70**, 024107.

59 R. Berthelot, B. Basly, S. Buffière, J. Majimel, G. Chevallier, A. Weibel, A. Veillère, L. Etienne, U.-C. Chung, G. Goglio, M. Maglione, C. Estournès, S. Mornet and C. Elissalde, *J. Mater. Chem. C*, 2014, **2**, 683-690.

60 W. L. Zhong, Y. G. Wang, P. L. Zhang and B. D. Qu, *Phys. Rev. B*, 1994, **50**, 698-703.

61 K. Uchino, E. Sadanaga and T. Hirose, *J. Am. Ceram. Soc.*, 1989, **72**, 1555-1558.

62 I. Ueda, M. Takiuchi, S. Ikegami and H. Sato, *J. Phys. Soc. Jpn.*, 1964, **19**, 1267-1273.

63 H. Lee, N. J. Smith, C. G. Pantano, E. Furman and M. T. Lanagan, *J. Am. Ceram. Soc.*, 2010, **93**, 2346-2351.

64 W. Huebner, S. C. Zhang, B. Gilmore, M. L. Krogh, B. C. Schultz, R. C. Pate, L. F. Rinehart and J. M. Lundstrom, *Proc. 12th IEEE Int. Pulsed Power Con.*, 1999, **2**, 1242-1245.

6. Figures Captions

Fig. 1 Schematic illustration of the formation of $BaTiO_3$/low melting glass core-shell nanoparticles: (1) dispersion of $BaTiO_3$ nanoparticles under ultrasonic agitation, (2) preparation of borosilicate precursor solution, (3) preparation of lead or bismuth precursor solution, (4) uniform distribution of precursors and $BaTiO_3$ base solution, (5) precipitation under base condition.

Fig. 2 TEM micrographs of (a) (b) as prepared $BaTiO_3$/PbO-B_2O_3-SiO_2 core-shell nanoparticles with various shell thicknesses (the arrows in (a) and (b) indicate the coating layer), (c) (d) as prepared $BaTiO_3$/Bi_2O_3-B_2O_3-SiO_2 core-shell nanoparticles with the shell region defined by arrows and dashed lines.

Fig. 3 XRD patterns of (a) $BaTiO_3$/PbO-B_2O_3-SiO_2 core-shell nanoparticles, and (b) $BaTiO_3$/Bi_2O_3-B_2O_3-SiO_2 core-shell nanoparticles with $BaTiO_3$ peaks labeled.

Fig. 4 FT-IR spectra of pristine $BaTiO_3$ (BT), lead borosilicate glass-coated $BaTiO_3$ (Pb-BT), and bismuth borosilicate glass-coated $BaTiO_3$ (Bi-BT).

Fig. 5 Sintered sample density as a function of temperature for Pb-BT composite and Bi-BT nanocomposite.

Fig. 6 SEM images of the fracture surfaces of (a) lead borosilicate glass-coated $BaTiO_3$ composite sintered at 700°C for 2 h (b) bismuth borosilicate glass-coated $BaTiO_3$ nanocomposite sintered at 900°C for 2 h (c) pristine $BaTiO_3$ sintered at 900 ℃ for 2 h.

Fig. 7 XRD patterns of (a) lead borosilicate glass-coated $BaTiO_3$ composite sintered sample (b) bismuth borosilicate glass-coated $BaTiO_3$ nanocomposite sintered sample.

Fig. 8 (a) Dielectric constant and (b) loss tangent of Bi-BT nanocomposite as a function of temperature.

Fig. 9 Weibull plot of dielectric breakdown strength in Bi-BT nanocomposite with thicknesses of 300 μm and 12 μm.

Fig. 10 (a) P(E) hysteresis loops of coarse-grained barium titanate (C-BT) and Bi-BT nanocomposite with 16 μm thickness, and (b) discharge energy density as a function of electric field for coarse-grained barium titanate (C-BT) (circles) and Bi-BT nanocomposite with 16 μm thickness (squares); dashed line shows the parabolic curve fitting for Bi-BT nanocomposite.

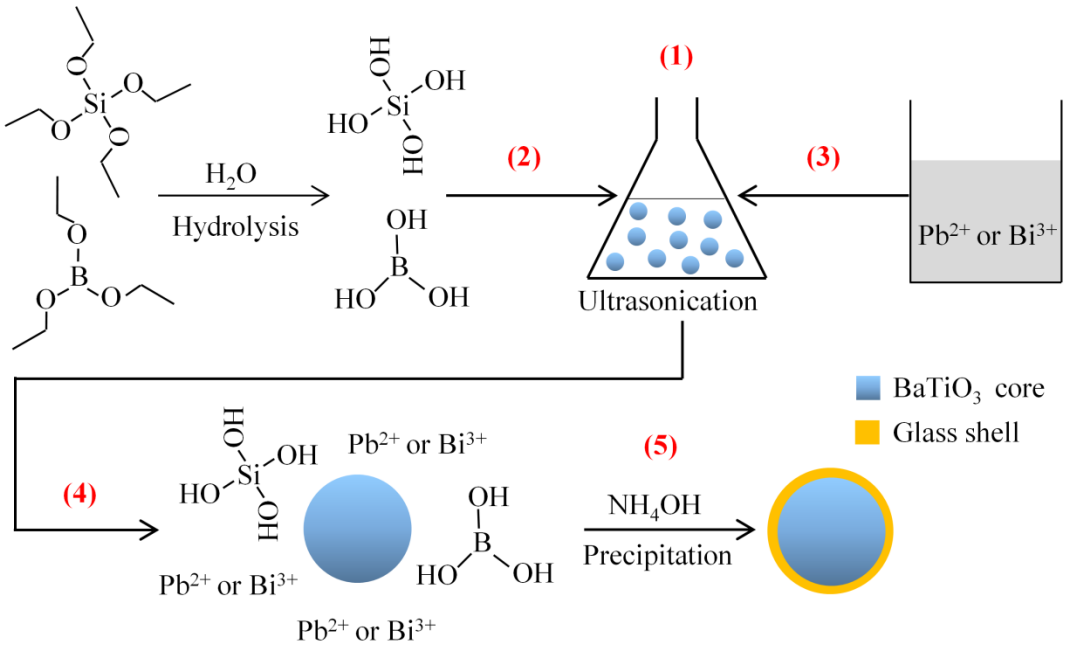

Fig. 1 Schematic illustration of the formation of $BaTiO_3$/low melting glass core-shell nanoparticles: (1) dispersion of $BaTiO_3$ nanoparticles under ultrasonic agitation, (2) preparation of borosilicate precursor solution, (3) preparation of lead or bismuth precursor solution, (4) uniform distribution of precursors and $BaTiO_3$ base solution, (5) precipitation under base condition.

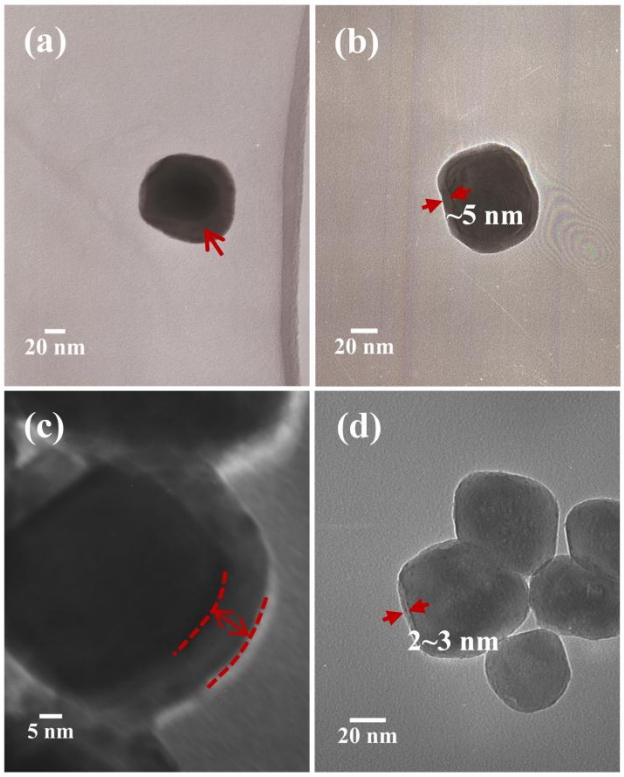

Fig. 2 TEM micrographs of (a) (b) as prepared $BaTiO_3$/PbO-B_2O_3-SiO_2 core-shell nanoparticles with various shell thicknesses (the arrows in (a) and (b) indicate the coating layer), (c) (d) as prepared $BaTiO_3$/Bi_2O_3-B_2O_3-SiO_2 core-shell nanoparticles with the shell region defined by arrows and dashed lines.

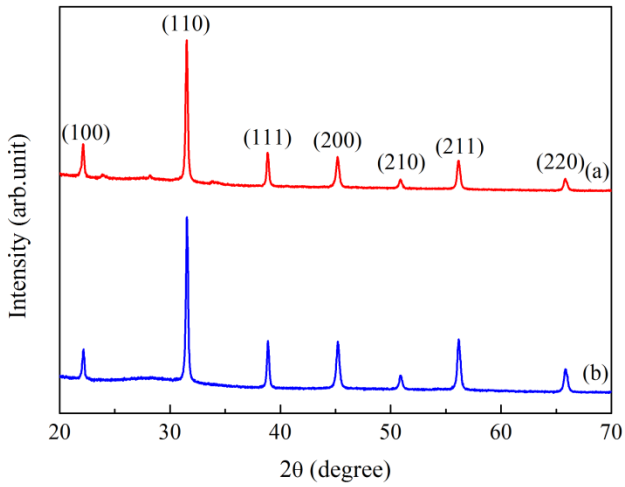

Fig. 3 XRD patterns of (a) $BaTiO_3$/PbO-B_2O_3-SiO_2 core-shell nanoparticles, and (b) $BaTiO_3$/Bi_2O_3-B_2O_3-SiO_2 core-shell nanoparticles with $BaTiO_3$ peaks labeled.

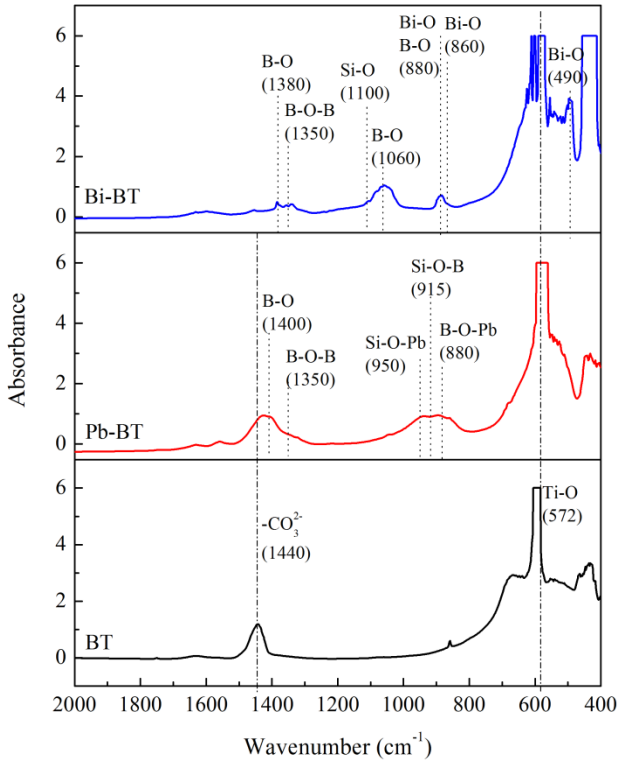

Fig. 4 FT-IR spectra of pristine $BaTiO_3$ (BT), lead borosilicate glass-coated $BaTiO_3$ (Pb-BT), and bismuth borosilicate glass-coated $BaTiO_3$ (Bi-BT).

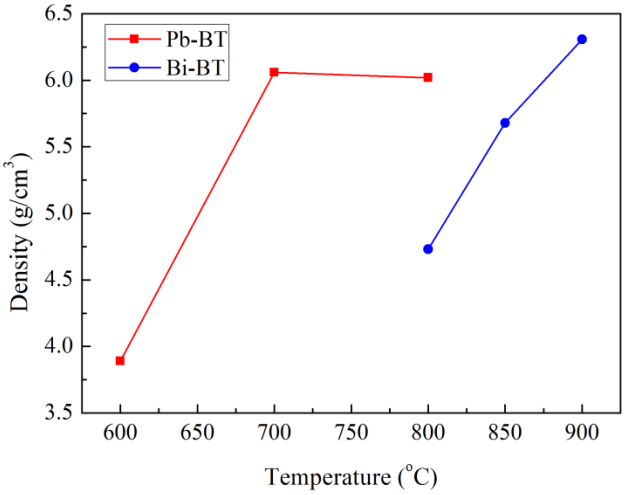

Fig. 5 Sintered sample density as a function of temperature for Pb-BT composite and Bi-BT nanocomposite.

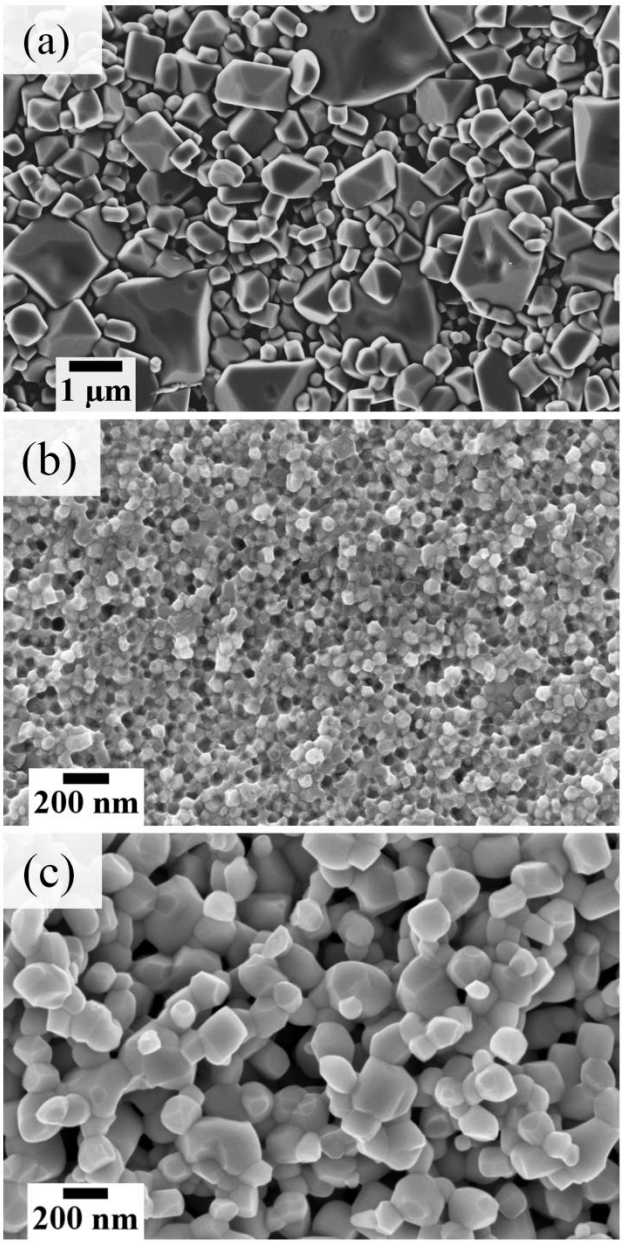

Fig. 6 SEM images of the fracture surfaces of (a) lead borosilicate glass-coated $BaTiO_3$ composite sintered at 700°C for 2 h (b) bismuth borosilicate glass-coated $BaTiO_3$ nanocomposite sintered at 900°C for 2 h (c) pristine $BaTiO_3$ sintered at 900 ℃ for 2 h.

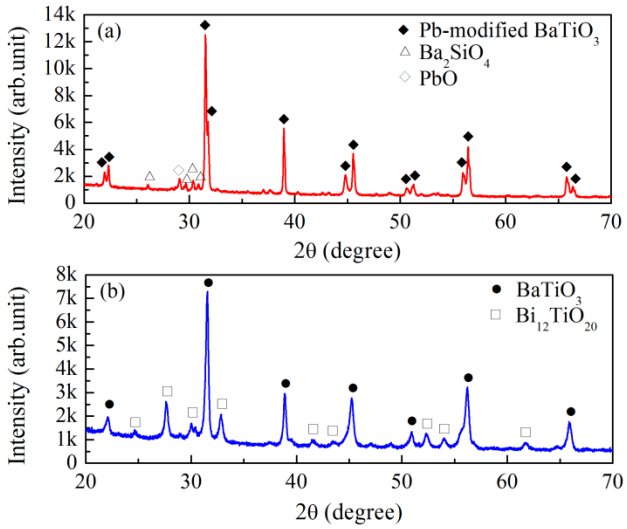

Fig. 7 XRD patterns of (a) lead borosilicate glass-coated $BaTiO_3$ composite sintered sample (b) bismuth borosilicate glass-coated $BaTiO_3$ nanocomposite sintered sample.

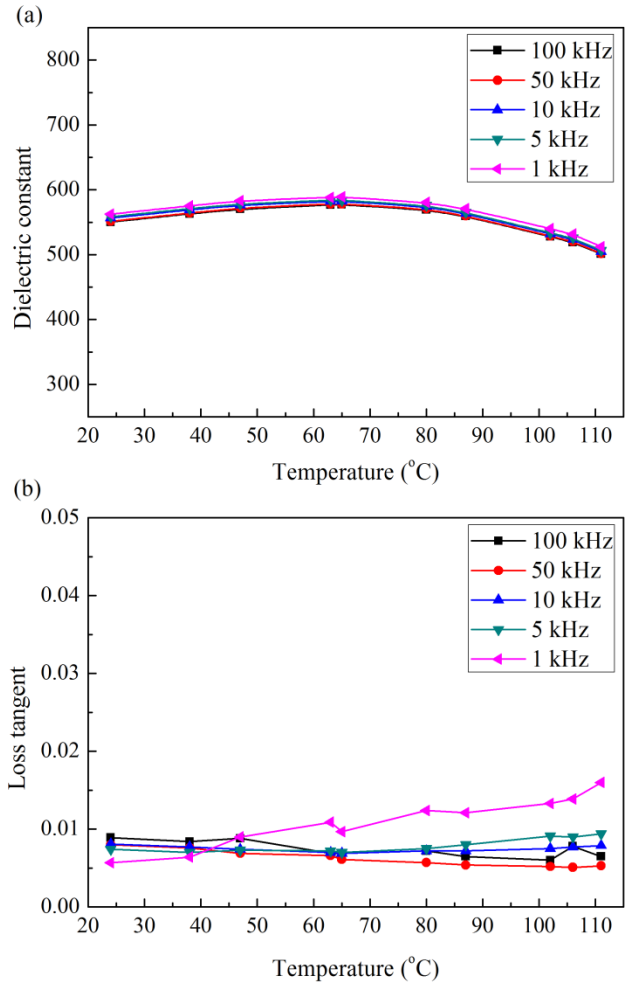

Fig. 8 (a) Dielectric constant and (b) loss tangent of Bi-BT nanocomposite as a function of temperature.

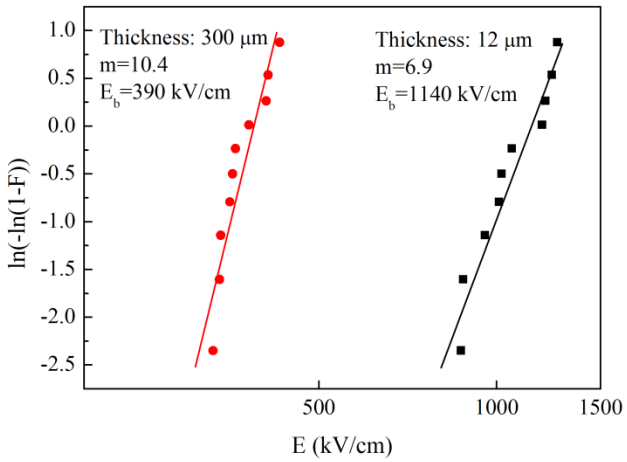

Fig. 9 Weibull plot of dielectric breakdown strength in Bi-BT nanocomposite with thicknesses of 300 μm and 12 μm.

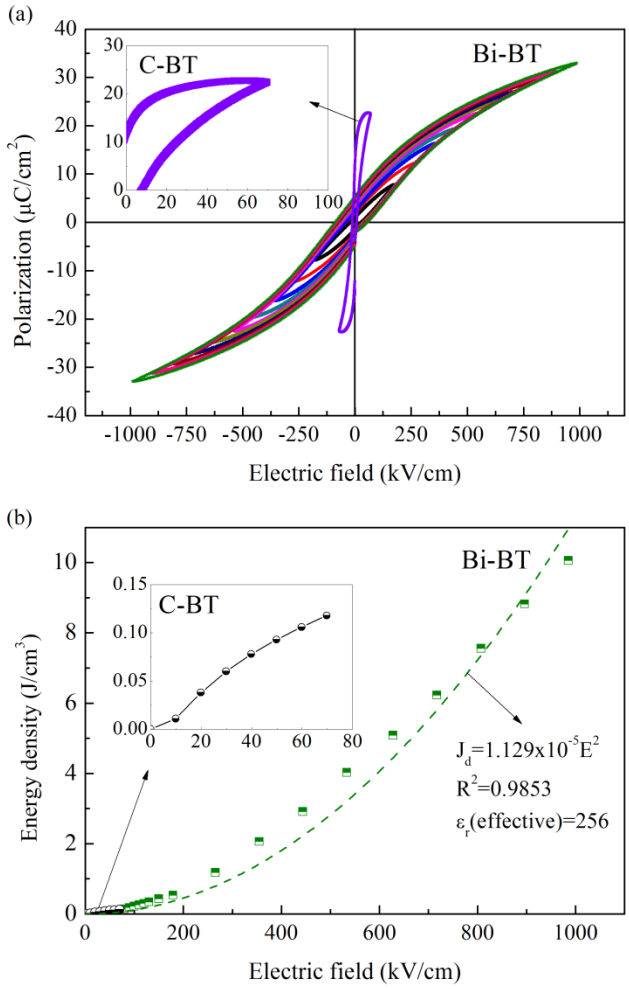

Fig. 10 (a) P(E) hysteresis loops of coarse-grained barium titanate (C-BT) and Bi-BT nanocomposite with 16 μm thickness, and (b) discharge energy density as a function of electric field for coarse-grained barium titanate (C-BT) (circles) and Bi-BT nanocomposite with 16 μm thickness (squares); dashed line shows the parabolic curve fitting for Bi-BT nanocomposite.